ORIGINAL PAPER

Electrochemical features of ball-milled lithium manganate spinel for rapid-charge cathodes of lithium ion batteries

**Daniel Crain · Jianping Zheng · Christopher Sulyma ·
Corina Goia · Dan Goia · Dipankar Roy**

Abstract Lithium manganese oxide (LMO), mechanochemically modified by ball-milling, is a potentially useful active material for high-power-density cathodes of lithium ion batteries. The present work investigates the electrochemical characteristic of a cathode prepared from a controlled mixture of nano- and micrometric LMO particles processed in this approach. The nanoparticles in the mixture support surface-localized insertion/extraction of Li and thus increase the cathode charge/discharge rates. The LMO microparticles promote cathode cyclability by stabilizing the coexisting nanoparticles against segregation and strong electrolyte reactions. The underlying mechanisms of these effects are studied here using voltammetry, galvanostatic cycling, Ragone plot construction, and electrochemical impedance spectroscopy. The relative timescales of charge transfer and diffusion of Li^+ within the LMO lattice are determined, and the criteria for material utilization during rapid charge–discharge are examined.

Keywords Ball-milling · Lithium ion battery · Lithium manganese oxide · Nanomaterial · Ragone plot

Introduction

Lithium ion batteries designed for pulse-power applications require that the electrode materials be capable of supporting fast intercalation/de-intercalation of Li^+. A widely practiced approach to achieving this goal is to use nano-sized particles of active materials, where the lithium insertion/extraction steps are accelerated by reducing the diffusion length of Li^+ within the host lattice [1]. Because intercalation/de-intercalation occurs primarily as "surface" (rather than bulk) reactions in such cases, the Li-host nanoparticles experience reduced volumetric stress of lattice deformation; this serves to increase both the cycle-life and the coulombic efficiency of the battery. However, while the increased specific area improves the rate capability and cyclability of electrode particles, this also makes the electrode more susceptible to segregation and/or modification by Faradaic reactions of electrolytes/impurities [2].

A viable option for boosting the power density, without sacrificing the electrochemical stability of an electrode, is to incorporate strategically designed mixtures of nanometric and micrometric active particles in the electrode film [3]. The micro-particles in such a mixture "protect" the nano-particles from electrolyte induced degradation, while the smaller particles promote fast charge/discharge. Mechanochemical processing via ball-milling of micrometric particles offers a broadly reported effective method to achieving such controlled size distributions of active particles [4]. Mechanical pulverization by ball-milling allows for particle size reduction of commercially obtained or chemically synthesized micro-structured materials. Ball-milling can also support mechano-chemically induced reactions on continuously renewed surfaces, leading to material modification at the nanoscale. These mechano-chemical reactions, dictated by a combination of milling variables, control particle size distributions, as well as the processes of alloying and new phase formation [5, 6].

Focusing particularly on the considerations for fast charge/discharge Li ion batteries, the present work

D. Crain · J. Zheng · C. Sulyma · D. Roy (✉)
Department of Physics, Clarkson University,
Potsdam, NY 13699-5820, USA
e-mail: samoy@clarkson.edu

C. Goia · D. Goia
Department of Chemistry, Clarkson University,
Potsdam, NY 13699-5810, USA

investigates certain electrochemical attributes of the ball-milled form of a cathode material, lithium manganese oxide (LMO, $LiMn_2O_4$). LMO has an adequate charge capacity and coulombic efficiency, as well as good rate capability and environmental compatibility [7–9]. Ball-milling has been shown to further improve several aspects of this material's cathode performance [4, 10]. Various structural properties and the main charge–discharge characteristics of ball-milled (BM)–LMO cathodes have been studied by other authors [5, 6, 11–13]. In a recent work, we have examined certain kinetic aspects of accelerated charge–discharge of LMO cathodes fabricated from BM particles [10]. In the present investigation, we extend our previously reported experimental strategy to study the relative times of the kinetically controlled and diffusion limited steps of Li intercalation/de-intercalation in BM–LMO. Using Ragone plots of energy–power correlation, we also examine here how the amount (effective thickness) of the utilized active material changes with variations in the charge/discharge rates (C-rates) and active particle sizes.

The cathode films are electrochemically characterized in half-cells using Li anodes in electrolytes of $LiBF_4$ (known for suppressing Mn dissolution [14]) in a mixture of ethylene carbonate (EC) and diethyl carbonate (DEC). The synergistic effects of different particle sizes in the BM material are probed with slow-scan cyclic voltammetry (SSCV), galvanosatic charge–discharge, and electrochemical impedance spectroscopy (EIS). The criteria for material utilization during fast charge/discharge are examined using Ragone plots of energy and power densities. EIS results are analyzed using the complex non-linear least square (CNLS) method to determine the voltage-dependent kinetic parameters of Li transport in the LMO cathodes. The relative timescales of charge transfer and Li^+ diffusion are determined from these EIS data.

Experimental

Cathode fabrication and test cell assembly

A slurry initially consisting of 10 g of LMO powder (Sigma Aldrich), 15 ml of 2-propanol (reagent-grade), and cerium-stabilized zirconium oxide beads of 1.2–1.4 mm diameter (Union Process) was ball-milled for 13.5 h at various rates to obtain a bimodal distribution of particles with 300 nm and 1.3 μm average diameters. Milling was performed using a vertical shaft-driven model HD-01 Attritor, and the resulting slurry was dried for 12 h in a vacuum oven at 80 C. Particle size distributions were monitored using a Malvern Mastersizer 2,000 analyzer. The cathode composite paste contained 80:13:7 weight percents of $LiMn_2O_4$/acetylene black/polyvinylidene fluoride in a base of N-methylpyrrolidone.

Alumina substrates were coated with Au (~1 μm thickness, served as a current collector) in a Denton cold sputter coater. A "doctor's blade" was used to coat the Au film with the LMO composite paste [2]. The resulting electrodes were dried in a vacuum oven for 24 h at 100 °C. The final electrodes typically contained about 0.7 mg cm^{-2} of active material. Micrographs of electrode samples were taken using a JEOL-JSM 6300 scanning electron microscope (SEM). The cathode film thicknesses were ~15 μm, as determined using SEM.

Electrochemical characterization

All electrochemical measurements used a three-electrode configuration with Li foils for the counter and reference electrodes and a working electrode of LMO. The Li salt was dried for 12 h at 70 °C in a vacuum oven, and the electrolyte, 1 M $LiBF_4$ in 1:1 (by volume) of EC/DEC was prepared with Fisher reagent-grade chemicals. The mixed electrolyte was dehydrated in a flask with dried 4 A molecular sieves (alumina–silicate, Fisher) for at least 12 h before use. The electrochemical test cell was assembled in a Terra Universal glove box with a Nitro Watch™ purging system, and the atmosphere inside the glove box was prepared by pumping dry air, followed by dry Ar, through a series of desiccator tubes containing activated molecular sieves and silica gel [15]. The experimental electrolyte was purged with ultra-high purity Ar for 30 min before electrode insertion.

Electrochemical measurements were carried out with freshly prepared electrodes and using a PAR-VersaSTAT3 potentiostat/galvanostat (for SSCV) or a 1287A Potentiostat (for galvanostatic and EIS experiments). Ragone plots were constructed using galvanostatic data recorded at a fixed 1-C rate of charge and variable rates of discharge. Each fresh cathode was discharged to 3.4 V to ensure a staring state of charge (SoC) of zero, and then galvanostatic charge/discharge measurements were performed at different rates between 3.4 and 4.2 V. In some of these experiments, the upper voltage limit was extended to 4.3 V to check the cut-off voltage necessary for complete cathode-charging. For EIS measurements, the cathode was subjected to intermittent galvanostatic charging (3.4–4.2 V) at a rate of (1/3)-C, and Nyquist spectra were recorded at several intermediate open circuit potentials (OCPs) after the electrode current completely dropped to zero. EIS was performed using a 15 mV rms AC perturbation voltage of frequencies ranging from 0.01 Hz to 100 kHz. The EIS data were validated by comparing the input and output frequency spectra and CNLS-analyzed using ZsimpWin™ to obtain electrode equivalent circuit (EEC) models. The calculated value of each EEC element had an uncertainty of <5% and, for reporting, was normalized with respect to the cathode's active material mass.

Results and discussion

Mechano-chemical processing of LMO powder

The distribution of particle sizes, monitored in terms of average particle diameters (d) at different stages of milling, are shown in Fig. 1. The initial size distribution was broad and centered at ~6 μm. Successively recorded size distributions show that, in 1.5 h, the peak of particle sizes narrowed to around 1.5 μm. After 4 h of milling, the particles had reached an average size of about 1.3 μm. Subsequent milling during the next 9.5 h was done at a nearly doubled speed of shaft rotation, which eventually resulted in a bimodal distribution centered at ~1.3 μm and ~300 nm. The shifting of size distributions after sonication indicated some degree of initial agglomeration, which was not present in the final dried powder. Sequentially taken SEM images, shown in Fig. 2, indicated how the particle morphologies evolved from relatively large and irregular to smaller, more uniform structures.

Cyclic voltammetry and Faradaic reactions of surface films

If an intercalation material is subjected to rigorous ball-milling, it is necessary to ensure that the intrinsic ability of
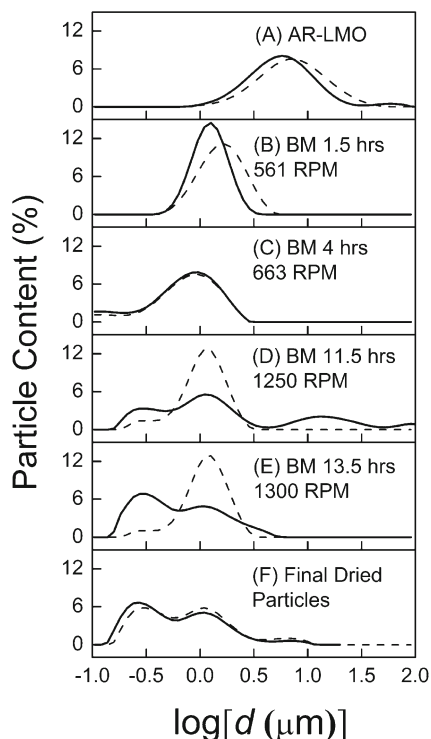

Fig. 2 **a–f** SEM images of LMO powder samples considered in the corresponding panels of Fig. 1

the sample for hosting Li$^+$ ions remains unaffected by the mechano-chemical processing conditions applied. This can be accomplished in a relatively straightforward way by using SSCV, where the cathode is charged and discharged under voltage control to probe its expected characteristic features. A primary signature of Li$^+$ insertion in LMO is that the reaction is a two-step Faradaic process [16]. The presence of these two reaction steps generally indicates adequate structural integrity of the host lattice and can be observed as clearly distinguishable current peaks in SSCV [17]. Slow potential scans used in such experiments allow for the time necessary to support solid-state diffusion of Li$^+$ and minimizes the double-layer currents. Figure 3a shows the results of SSCV experiments, obtained by applying two consecutive voltage cycles at a rate (v) of 25 μVs^{-1} to a cathode prepared from the BM–LMO particles shown in Fig. 2f.

The left vertical axis in Fig. 3a represents the cell current (i) plotted against the applied cell voltage (E) and normalized with respect to the cathode's active material mass. The intercalation/de-intercalation reactions that lead to this current have the following general form [18].

$$[h^{-\delta} + Li^{+\delta}] \rightleftharpoons Li^+ + [h^0] + e^- \tag{1}$$

where $[h^0]$ is the empty host lattice site and e$^-$ denotes electrons; $+\delta$ is the partial charge on the intercalated Li$^+$

Fig. 1 Evolution of average particle diameters (d) of LMO powder, sequentially obtained at various stages of ball-milling using different shaft speeds (*RPM*). **a** All-micrometric, AR–LMO. **b–c** LMO at different stages of milling; (**d**) final dried particle size distribution. The *dashed* and *solid* lines correspond to LMO particles before and after sonication of the samples, respectively
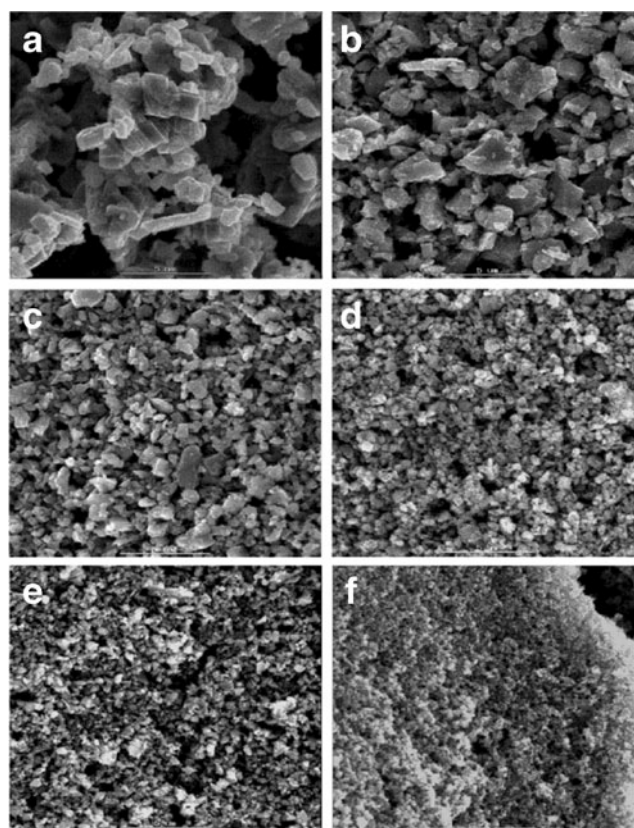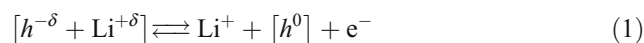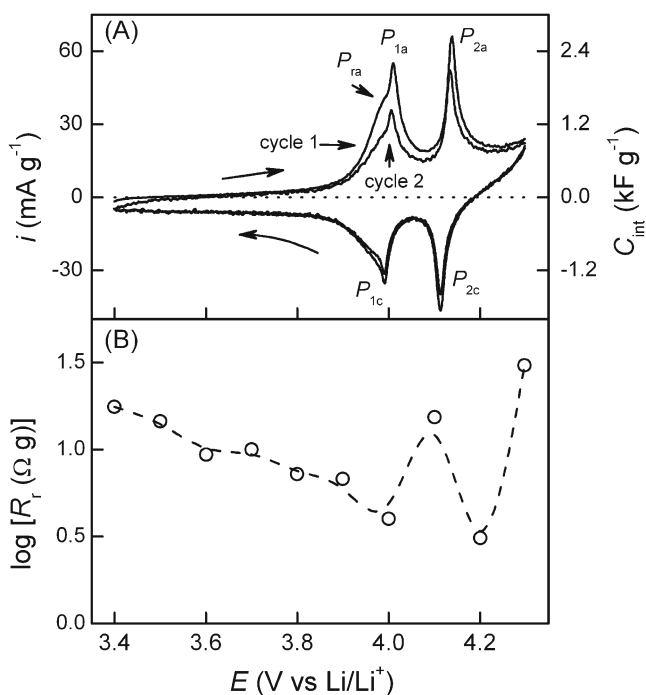
Fig. 3 **a** Current (i) and intercalation capacitance (C_{int}) of a BM–LMO cathode, recorded during the first two SSCV cycles performed at a scan rate of 25 μVs^{-1} using an electrolyte of 1 M LiBF$_4$ in 1:1 (volume) EC/DEC. The current feature P_{ra} arises from electro-oxidation of cathode surface films. P_{1a} and P_{2a} represent signature features of phase transition in the host lattice during anodic de-intercalation of Li$^+$. P_{1c} and P_{2c} are the corresponding cathodic current peaks of Li$^+$ intercalation. **b** Faradaic reaction resistance R_r of the surface film of LMO

and $-\delta$ is the opposite charge associated with the intercalation site. The left-hand side of Eq. 1 corresponds to a fully charged LMO cathode and, on the right-hand side, $[h^0]\equiv 2(\lambda-MnO_2)$. The two current peaks, marked as P_{1a} and P_{2a} in the anodic cycle of Fig. 3a show the expected two-step process of Li$^+$ extraction from LMO [17, 19]. The cathodic counterparts of these current features are labeled as P_{1c} and P_{2c}, respectively.

At voltages below the location of P_1, reaction (1) occurs within a single cubic phase of LMO, where the SoC (x) is less than 0.5. At higher voltages, where $0.5<x<1$, the LMO lattice acquires a two-phase structure and gives rise to the second current peak P_2. In the forward (charge) direction of reaction (1), the LMO particles have more Li in their cores than in their surface regions, and the situation is reversed during the discharge step. These mutually disparate concentration profiles of Li$^+$ developed within the LMO particles during charge and discharge of the cathode causes a hysteresis between the forward and backward activations of reaction (1) [20]. As a result, the cathodic current peaks in Fig. 3a are somewhat shifted toward lower voltages with respect to their corresponding anodic peaks. These are signature features of Li intercalation/de-intercalation in LMO, and the detection of these features in Fig. 3a confirms that

the LMO after milling retains its usual intercalation characteristics.

A relatively small anodic current peak, labeled P_{ra}, is observed in the first-cycle voltammogram of Fig. 1a. Based on earlier reported observations [21–23], this peak can be associated with Faradic reactions of the native cathode surface films (CSFs) [2, 10]. This current most likely comes from irreversible anodic oxidation of Li–EC complexes contained in the surface films formed on LMO. This CSF reaction disappears after the first anodic scan and remains absent in all successive cathodic and anodic voltage cycles. Due to this reason, the total anodic current drops from cycle 1 to cycle 2. As shown previously, the CSF reaction current (i_r) can be estimated by writing $i_r\approx$(cycle 1)$-i$ (cycle 2). The Faradaic resistance, R_r, of the CSF reaction can be determined from i_r by using the definition, $R_r=(di_r/dE)^{-1}$. Voltage-dependent values of [log (R_r)], obtained in this approach using the data of Fig. 3a, are shown in Fig. 3b (symbols) where the dashed line indicates the overall data-trend.

The plot of R_r in Fig. 3b shows two noticeable dips at the voltages corresponding to the two steps of Li de-intercalation from LMO. This suggests that CSF oxidation occurs at its highest rate during Li extraction from the cathode and hence, most likely involves the release of Li$^+$ ions. The mechanism of this CSF reaction has been proposed previously, suggesting that the CSF, composed primarily of a Li–EC complex, oxidizes with simultaneous releases of C$_3$H$_4$O$_3$ and Li$^+$ in the electrolyte [15]. The values of R_r measured here for the BM–LMO sample is about an order of magnitude larger than those measured previously under similar conditions using a cathode of micron-sized LMO particles [2].

Galvanostatic charge/discharge of cathodes

The cyclability and rate capability of the BM–LMO material were compared with those of all-micrometric LMO through a series of galvanostatic charge/discharge experiments performed at different rates between 0.3-C and 10-C. Illustrative results of these measurements are presented in Fig. 4, where panels a and b show capacity vs. voltage plots of AR–LMO and BM–LMO for three successive cycles, maintained at a 0.3-C rate of electrode cycling, respectively. In Fig. 4c, the BM sample is charged/discharged at 10-C. In all three panels, the plots corresponding to cycles 1, 2, and 3 are labeled accordingly.

The right-most data point on each plot in Fig. 4 represents the maximum experimentally available capacity, C_m, for the given sample under the corresponding experimental conditions. For porous cathode films, $C_m = f_0 C_{Th}$, where C_{Th} is the theoretical charge capacity of LMO; $C_{Th}=(F/M)=148$ mAh g^{-1}; F and M are the Faraday constant and the molar mass of LMO, respectively. The fraction f_0 is defined as [24]:

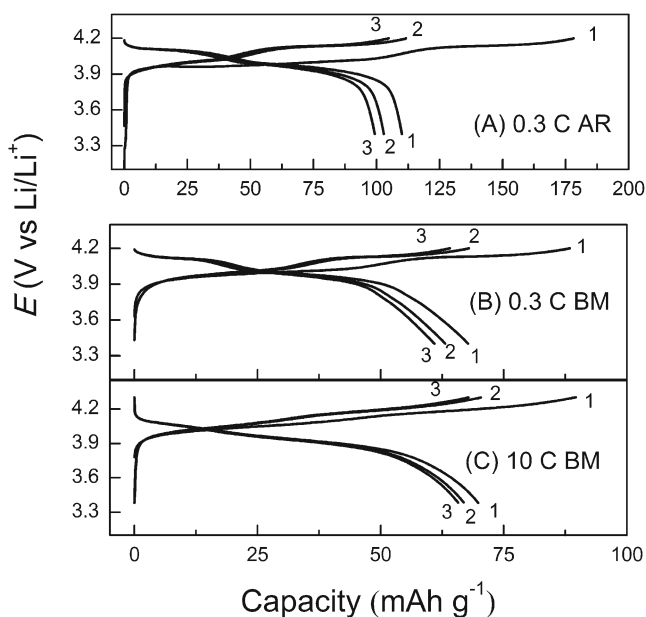$$f_0 = n_h(1-\phi)LM(m_0)^{-1} = C_m(C_{Th})^{-1} < 1, \quad (2)$$

Fig. 4 Charge/discharge plots for LMO cathodes prepared with **a** all-micrometric and **b**, **c** BM materials. The three *upper* and *lower* sets of plots represent charge and discharge steps of the first three galvanostatic cycles of fresh samples, respectively. The cycle numbers and C-rates are indicated

where n_h is the density of empty host sites $[h^0]$ available in the cathode film to support reaction (1); ϕ and L are the porosity factor and thickness of the cathode film, respectively; m_0 is the area-normalized mass of LMO in the cathode.

According to Fig. 4a, b, at the relatively slow 0.3-C rate of cycling the AR–LMO cathode exhibits a higher value of C_m. This is expected because mechano-chemical effects tend to partially oxidize Mn and decrease the Li-content of BM–LMO [25]. Thus, the term n_h in Eq. 2 acquires a comparatively lower value for the BM sample, which acts to limit the maximum available capacity of the sample [11]. Despite its initially constrained values, the capacity of the cathode in Fig. 4b fades at a relatively lower rate. In particular, the first-cycle capacity loss, which is associated mostly with CSF reactions, is comparatively less drastic for BM–LMO. This is consistent with the rather large values of R_r observed in Fig. 3b for BM–LMO. At increased cycling rates, the charge capacity of the AR–LMO cathode was found to drop noticeably, whereas that of the BM–LMO cathode decreased by lesser amounts under the same conditions. Sample results for the latter case are presented in Fig. 4c, showing that, even after a >30-fold increase in the C-rate, the capacity of the BM–LMO cathode remains nearly unchanged with respect to its values observed in Fig. 4b. Because the voltage range (3.4–4.2 V) used in Fig. 4b was slightly smaller than that (3.4–4.3 V) in Fig. 4c, the capacities measured in the latter case typically exhibited a small increase (3–5%) in their values. Nevertheless, the general level of capacity retention for BM–LMO remained essentially unchanged between 0.3-C and 10-C.

The electrochemical performance of BM–LMO observed under the conditions of rapid charge/discharge is rooted in the fast transport of Li$^+$ within the nano-metric constituent of this material. To illustrate this point, we note that the net rate of reaction (1) is dictated by the timescale of slow (solid state) diffusion of Li$^+$ in the LMO matrix. The characteristic diffusion time, $\tau_d^{(o)}$, of Li in an active particle has the form [10, 26]:

$$\tau_d^{(o)} = (l_d)^2 (\widetilde{D})^{-1}, \tag{3}$$

where l_d is the Li$^+$ diffusion length, which corresponds to the dimension of the active particle. $\widetilde{D}$ is the chemical diffusion coefficient of Li$^+$ in LMO. According to Eq. 3, the diffusion time of Li$^+$ is considerably reduced as the LMO particle size is reduced from micro- to nano-scale [23]. Furthermore, the value of $\widetilde{D}$ for a nanoparticle host is larger than that for a micro-particle, because the diffusion channels are restricted in the former case [1]. These attributes of the nanosized active particles enhance the cathode's charge/discharge rate capability.

Galvanostatic charge/discharge characteristics of the BM–LMO and AR–LMO cathode samples were also tested under the conditions of extended cycling, using 50 repeated cycles at a rate of 3-C (detailed results not included here). Cumulatively, the BM–LMO exhibited a 90% capacity retention over 50 cycles in comparison with a 76% retention for the all-micrometric sample. However, the coulombic efficiencies, calculated as $[C_m$ (discharge)/C_m (charge)] from the 3-C galvanostatic data, were quite comparable between the two samples, with a consistently fixed value of 99.2% over 50 cycles.

The Li-host nanoparticles experience reduced volumetric stress of lattice deformation, because intercalation/de-intercalation occurs primarily as surface-localized reactions. This serves to improve both the cycle-life and the coulombic efficiency of the electrode. The larger LMO particles included in the cathode film support chemical and structural stabilities of the film by restricting electrolyte reactions and segregation of smaller particles in the mixture [10]. Thus, the bimodal particle-size distribution of the BM–LMO found in Fig. 1f plays a major role in improving the rate capability and cyclability for this sample.

Correlation between energy and power densities

The gravimetric specific energy, ε_s, of a battery electrode is obtained as a product of the open circuit voltage and the specific charge capacity of the cell. The average specific power, P_s, delivered by the battery while charging, or extracted from the battery while discharging the cell is given by the ratio, ε_s/T_{exp}. Here, T_{exp} denotes the total charge or

discharge time experimentally set by the C-rate, which, in the galvanostatic mode, is done by selecting a predetermined value of the electrode-area normalized discharge current, i_g. The energy available from the cell at a given C-rate depends on the relative values of T_{exp} and the net diffusion time of Li in the capacity-limiting electrode. Thus, the usable charge capacity of the electrode is given as $C_m(\text{used}) = [(i_g T_{exp})/m_0]$.

The diffusion time defined in Eq. 3 is based on the considerations of a single active particle. To estimate the overall time scale of Li diffusion in the context of material utilization of a full electrode, it is appropriate to generalize the single-particle diffusion length to the following form [24]:

$$L_{eff} = n_h V_M (1 - \phi) L = m_0 V_M C_m (F)^{-1}, \tag{4}$$

Where L_{eff} is the effective length that has to be travelled by intercalating ions within the cathode to fully utilize the available host sites; V_M is the molar volume of the active material. The condition for full utilization of the energy stored in the electrode can be written as:

$$T_{exp} > \tau_d = \frac{(L_{eff})^2}{\tilde{D}}, \tag{5}$$

Where τ_d is the minimum diffusion time necessary for Li transport to completely charge or discharge the whole electrode. This condition places a restriction on the lower limit of T_{exp} and hence on the upper limit of P_s that is available from an electrode specified by a given pair of C_m and ε_s. This correlation between P_s and ε_s can be examined with Ragone plots [27].

Figure 5 shows Ragone plots, recorded using the same electrolyte composition, for two electrodes prepared with (a) AR–LMO and (b) BM–LMO particles. In each case, the experimental cathode was subjected to repeated galvanostatic discharge cycles at variable rates between 1-C and 30-C following a fixed 1-C rate charging. The specific energies were determined by numerically integrating E vs. C plots of the discharge cycles. The diagonal lines indicate the discharge times (T_{exp}) associated with selected data points. At low values of P_s, variations in ε_s for both the BM- and the AR-LMO samples are relatively insensitive with respect to increasing the power output. In this region, ε_s for AR–LMO is somewhat larger than that of BM–LMO, because, as already noted in Fig. 4a, b, the specific capacity for the former is comparatively larger under the condition of slow discharge. However, under the conditions of fast discharge (log P_s>3 W kg^{-1}), the BM–LMO cathode exhibits its noteworthy electrochemical performance by providing relatively high energy densities available for utilization. While a large absolute capacity of the electrode in a Li ion battery is essential for high-energy-density applications, the rate capability serves as a critical electrochemical characteristic of cathodes for high-power-density applications. The
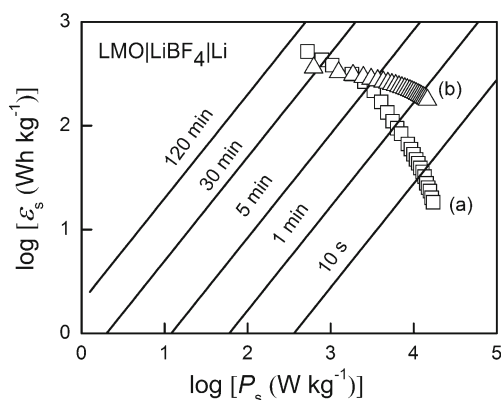

Fig. 5 Ragone plots of specific energy (ε_s) vs. specific power (P_s), recorded for *a* all-micrometric and *b* BM–LMO cathodes using galvanostatic charge (1-C rate) and discharge (variable rates between 1 C and 50 C) experiments performed in LMO|Li cells

Ragone plots in Fig. 5 illustrate the usefulness of the BM approach to electrode fabrication in such cases.

At T_{exp} <5 min, plot (a) in Fig. 5 begins to curve down noticeably, indicating that the condition specified in Eq. 5 is no longer met for this case at such fast rates of power consumption. On the other hand, plot (b) for the BM–LMO stays reasonably flat at even lower values of T_{exp}, demonstrating that Eq. 5 continues to hold for this sample during increased power delivery by the half-cell. As shown elsewhere [10], $\tilde{D}$ for the BM–LMO is considerably larger than that of the all-micrometric LMO. This promotes fast charge/discharge of BM–LMO, while maintaining the condition of active material utilization according to Eq. 5.

The relatively smaller volume-specific surface areas of micrometric LMO particles can cause a drop in the surface voltage as concentration polarization builds up during rapid charge/discharge. This also contributes to the lowering of ε_s in the high-power regime of plot (a) in Fig. 5. The nanoparticle constituents of BM–LMO, which determine the shape of plot (b) are mostly free of such concentration polarization effects. The Ragone plot for the BM–LMO eventually begins to drop in ε_s when T_{exp} is lowered below 1 min. This suggests that τ_d for the BM sample should be on the order of this time scale. More details of this specific point are addressed later in the present report using EIS results.

Nyquist spectra and impedance parameters

Figure 6 shows Nyquist impedance spectra for a BM–LMO cathode, collected using EIS at various open circuit potentials in the main potential region of intercalation/de-intercalation during the first two cycles of charge and discharge. Z' and Z'' denote the real and imaginary parts of the cathode impedance, respectively. The perturbation frequencies decrease from left to right along the Z' axis. Compared with

earlier reported results for all-micrometric LMO [2], the overall impedance of BM–LMO obtained here is substantially reduced, and indicates more efficient Li^+ transport in the latter case. Because the EIS measurements correspond to equilibrium conditions, the data collected during the charge and discharge cycles are mutually similar. The results are also similar between the first and second cycles due to the robust cyclability of BM–LMO. Voltage-sensitive variations in the Warburg impedance of Li diffusion are noticeable in the low-frequency (10−0.01 Hz) spectra. At the outer edges of the intercalation voltage region, these diffusion features are at their maximum values and are minimized during intercalation. The high-frequency arcs are due to the CSF.

The lines in Fig. 6 are CNLS calculated fits to the data, which lead to the EEC model shown in Fig. 7a. This EEC has been extensively used to describe surface reactions of various metal oxide cathodes for Li ion batteries [28–30]. The uncompensated electrolyte resistance R_u is essentially voltage-independent in the present experiments with an average value of 12.1 Ω g. Q_f and R_f denote the constant phase element (CPE) and the net resistance of the CSF, respectively. C_{dl} is the double-layer capacitance of the cathode. W is the Warburg element for Li^+ diffusion in the cathode, and R_{ct} is the charge transfer resistance for reaction (1); C_{int} is the intercalation capacitance of LMO.

The impedance of the Warburg element has the form: $Z_w = \sigma(1 - j)\omega^{-1/2}$, where ω is the angular frequency of AC perturbation, $j = \sqrt{-1}$, and σ is a frequency-independent diffusion parameter [10, 22, 28]: $\sigma = [V_M/(F\sqrt{2\widetilde{D}})]|dE/dx|$.

In the context of material utilization of electrodes [31], $x \approx (C/C_m)$, so that $\sigma = (V_M C_{Th})[F\sqrt{2\widetilde{D}}(dC/dE)]^{-1}$, where C is the charge capacity of the cathode [2, 10]. Using the definition, $C_{int}=m_0(dC/dE)$, one can express σ as:

$$\sigma = \frac{V_M m_0 C_m}{F C_{int} \sqrt{2\widetilde{D}}}, \tag{6}$$

where C_{int} is in its gravimetric unit. The voltage dependence of σ, plotted in Fig. 7b, is reversible with respect to charge/discharge as well as with respect to repeated cycling of the cathode. In addition, σ displays two dips at 3.95 and 4.15 V, corresponding to the current peaks seen in Fig. 4. Similar results for σ have been previously reported for LMO cathodes [32].

The C_{dl} vs. E plot in Fig. 8a shows a broad minimum between 4.0 and 4.1 V, which probably corresponds to the effective potential of zero charge of the carbon-containing part of the electrode. If the charge transfer step of reaction (1) is kinetically controlled, R_{ct} should have its minimum values converged around $x=0.5$ (expected at intermediate voltages) and should acquire larger values at $x\approx 0$ and 1, at the lower and upper voltage limits of the intercalation region, respectively [10]. The plot of R_{ct} in Fig. 8a appears to include the lower- and mid-sections of such a plot. According to Fig. 4, the maximum SoC for the BM–LMO sample does not reach a value of 1, and hence, the expected increase of R_{ct} in the higher voltage region (at $x>0.5$) is not observed here. Nevertheless, the data plotted in Fig. 8 for the separate charge and discharge cycles are concurrent and demonstrate the highly reversible nature of electrode cycling.

Fig. 6 Nyquist impedance plots for BM–LMO recorded at different OCPs. The cell voltage was changed galvanostatically at a rate of 1/3-C, and the electrode was allowed to equilibrate at the resulting OCP prior to EIS measurements. The *symbols* and the *lines* denote experimental data and CNLS fits to the data, respectively
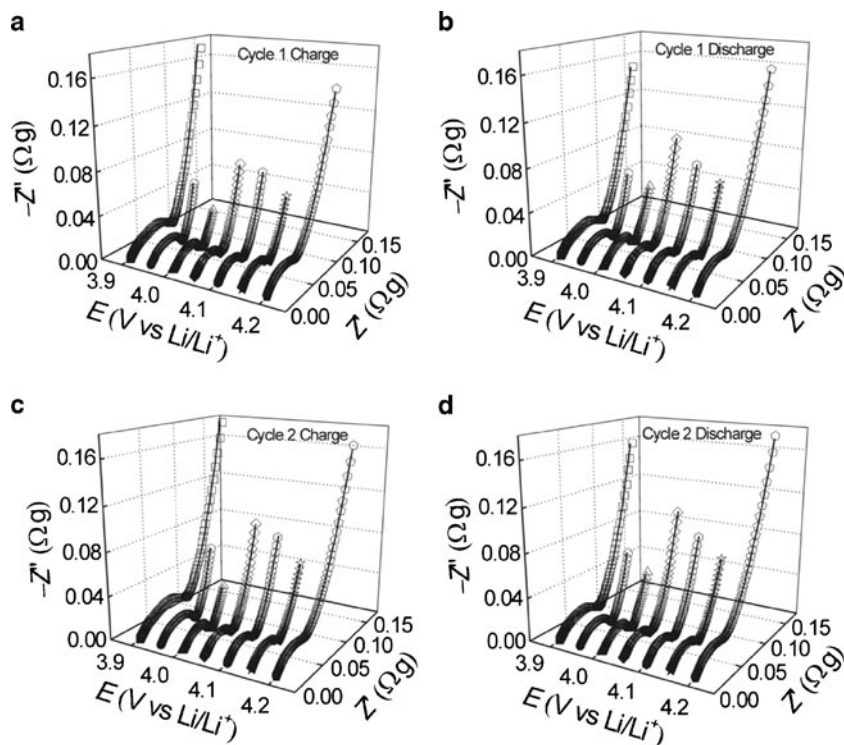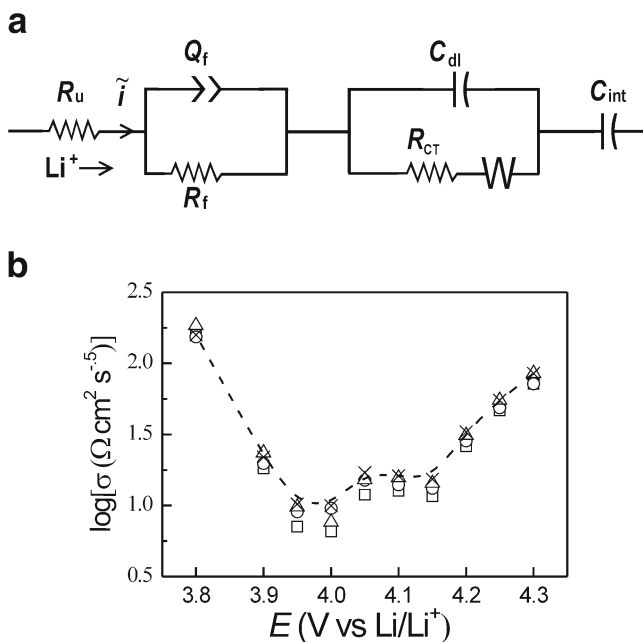
Fig. 7 **a** Electrode equivalent circuit model of the BM–LMO cathodes used in this work. **b** Diffusion impedance parameter σ (denoted by *symbols*) of BM–LMO, recorded during the first two charge and discharge cycles. The *line* shows the general trend of the data

Figure 9a shows the results for C_{int} obtained from EIS measurements at intermediate OCPs during the first and second galvanostatic charge/discharge cycles of a BM–LMO cathode. The symbols are data points, and the solid line shows the general trend of the data indicating two distinctly separated peaks. The voltages matching these peaks correspond to those of the current peaks observed in Fig. 3a and are associated with the two-step intercalation/de-
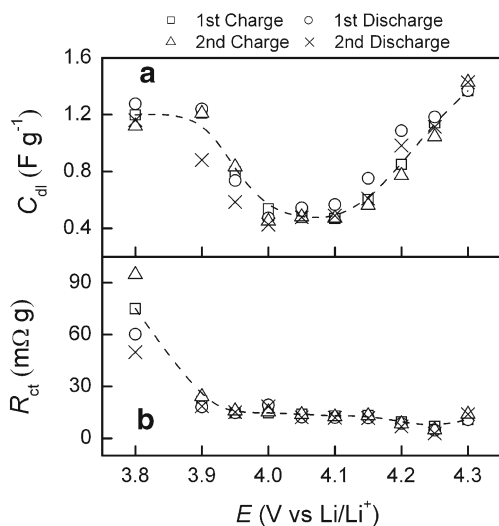
intercalation of Li in LMO. For comparison with these EIS results, in Fig. 9b, we plot C_{int} obtained from the second SSCV cycle (where $i_r=0$) of Fig. 3a. These latter data (symbols) represent the cycle-averaged quantity, $C_{int}=[(i_a/v)+(|i_c|/v)]/2$, where i_a and i_c are the anodic and cathodic currents of SSCV for the charge and discharge cycles, respectively; $v=(dE/dt)$. The dashed line in Fig. 9b represents the general inclination of C_{int} determined from SSCV, which agrees well with the corresponding EIS results in Fig. 9a.

Voltage-dependent values of $\tilde{D}$ for Li$^+$ in BM–LMO were determined by using the formulation of Eq. 6 and combining the data for σ and C_{int} from Figs. 7b and 9a, respectively. In the context of EIS-based measurements of $\tilde{D}$, it is customary to take the SoC of the electrode as the ratio (C/C_{Th}) [31–34]. We use this convention to determine $\tilde{D}$ from σ, which maintains an internally consistent framework for comparing the present results with those previously reported using the same approach for similar systems [10, 32]. The values of $\tilde{D}$ obtained in this way are presented in Fig. 9c, where the different symbols represent the first two charge and discharge cycles of a fresh cathode. The general trend of $\tilde{D}$, indicated by the solid line, is similar to that previously observed for BM–LMO in LiClO$_4$/EC/DEC electrolytes [10]. The two minima observed in the plot of $\tilde{D}$ appear at the voltages corresponding to the two phases of Li intercalation/de-intercalation that have already been
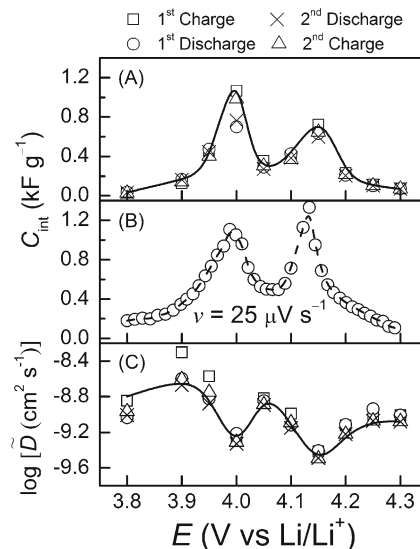

Fig. 8 **a** Double-layer capacitance (C_{dl}) and (**b**) charge transfer resistance (R_{ct}) of a BM–LMO cathode measured during the first two charge/discharge cycles. The *line* shows the general trend of the data denoted by the *symbols*

Fig. 9 Intercalation capacitance (**a** and **b**) and chemical diffusion coefficient (**c**) of a BM–LMO cathode measured in the voltage region of Li intercalation/de-intercalation. EIS results for the first two galvanostatic charge/discharge cycles are shown in **a** and **c**. **b** Shows SSCV results, averaged from the positive and negative voltage scans in Fig. 3a

observed in the results of Figs. 4a and 9a, b. The values of $\tilde{D}$ in Fig. 9c are more than an order of magnitude larger than those previously reported for micrometric AR–LMO particles [2]. These enhanced values of $\tilde{D}$ for the BM–LMO can be attributed to the largely surface-confined nature of reaction (1) in the nanometric particles [1].

Figure 10 shows the voltage-dependent impedance parameters measured for the CSF formed on BM–LMO during the first two charge/discharge steps of a fresh cathode. The lines through the symbols indicate the data-trends. The strong convergence of the different symbols shows once again the reversible nature of the EIS measurements. The CSF resistance R_f plotted in Fig. 10a represents a parallel combination of the Faradaic resistance R_r, and a nonfaradaic resistance R_{f0} of the surface complex. The observed values of R_f are controlled primarily by those of R_{f0}, because R_f in Fig. 10a is significantly smaller than R_r plotted in Fig. 3b. R_{f0} represents, in essence, an ohmic element, because its value is determined primarily by the thickness/porosity rather than the activity of the Li$^+$-conducting CSF film [10]. However, the CSF thickness and hence R_{f0} depends on the voltage-dependent reaction resistance R_r. A considerable dip occurs in the plot of R_f in the voltage region of reaction (1), where the lowest values of R_r also occur in Fig. 3. This shows how the CSF acquires its weakest structural configuration when its Faradaic oxidation occurs at a high rate.
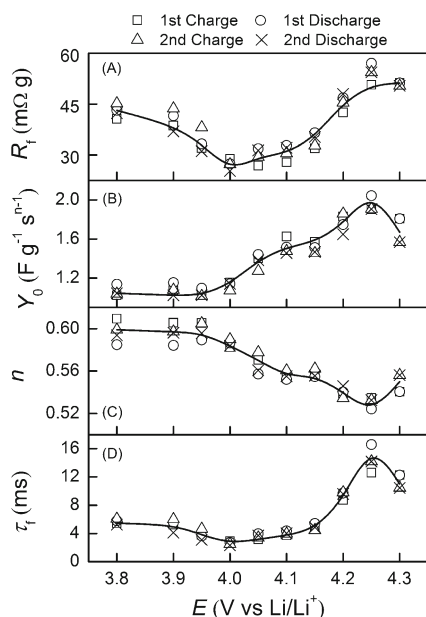
The impedance (Z_Q) of Q_f has the form $Z_Q = [Y_0(j\omega)^n]^{-1}$, where Y_0 and n are the characteristic CPE parameters, with $0 \leq n \leq 1$. If the electrode surface becomes spatially more inhomogeneous, then n decreases and Y_0 increases [35]. As the intercalation voltage region is approached from lower voltages, Li transport through the CSF increases, which, apparently increases the spatial in-homogeneity of the CSF in this region. This is indicated by the increasing values of Y_0, coupled with a correspondingly decreasing n along the positive voltage axis in Fig. 10a. In addition, adsorption of BF$_4^-$ anions from the electrolyte onto preferential sites of the CSF can reduce the spatial homogeneity of the latter [2]. Since this anion adsorption is expected to increase along the direction of anodic potentials, such an effect may also contribute to the observed voltage dependencies of the CPE variables.

The CSF parameters from Fig. 10a–c are combined in Fig. 10d, where the site-averaged structural relaxation time τ_f of the CSF is plotted by using the empirical definition [32], $\tau_f = (R_f Y_0)^{1/n}$. With increasing voltages in the intercalation region, τ_f closely follows the trend of Y_0. This implies that the CSF's electrical response becomes similar to that of a weakly charge-leaking capacitance when large numbers of Li$^+$ ions are transported through the CSF. Nevertheless, the values of τ_f fall mostly in the millisecond regime, representing a surface process significantly faster than Li extraction/insertion (T_{exp}) in the cathode. Therefore, the CSF does not have major effects on the cathode's intrinsic charge/discharge attributes.

Relaxation times for lithium intercalation/de-intercalation

The lithium intercalation/de-intercalation reaction, which involves diffusion of Li$^+$ in the host material, followed by charge transfer according to Eq. 1, is rate-limited by the
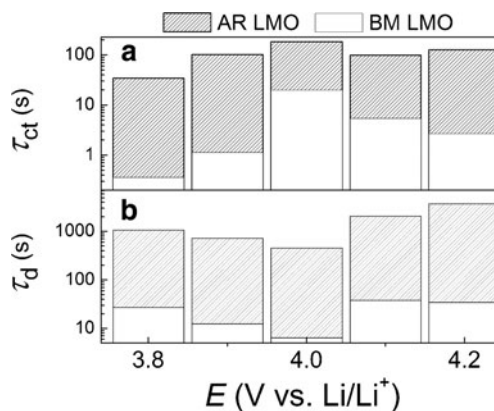
Fig. 10 Impedance parameters of the surface film formed on a BM–LMO cathode. The *symbols* correspond to the first two charge and discharge cycles, and the *lines* show the overall shapes of the plots. The parameters in **a–c** are obtained directly from CNLS analysis of experimental Nyquist spectra. In (*d*), τ_f is evaluated by combining the data from **a–c**

Fig. 11 **a** Charge transfer and **b** diffusion times for Li intercalation/de-intercalation measured with EIS at various open circuit voltages of AR–LMO (*shaded bars*) and BM–LMO (*open bars*) cathodes. The results shown here correspond to the first discharge cycle of a freshly prepared cathode

diffusion step—that is, by τ_d defined in Eq. 5. The relative timescales of these charge transfer and diffusion steps of Li transport in the cathode film can be estimated from the EIS measured kinetic parameters of the system. The relaxation time (τ_{ct}) of charge transfer in intercalation/de-intercalation can be obtained as $\tau_{ct} = R_{ct}C_{int}$. This empirical definition of τ_{ct} includes the time associated with the formation of the intercalation capacitance. Similarly, according to Eqs. 4 and 5, $\tau_d = [V_M m_0 C_m (F\sqrt{\widetilde{D}})^{-1}]^2$. By combining this expression with the formula for D in Eq. 6,

$$\tau_d = 2(m_0 \sigma C_{int})^2, \tag{7}$$

which appears as the diffusion time considered in the Lorenz Möckel treatment of slow interfacial reactions [36].

Experimental values of τ_{ct} for BM–LMO were obtained by combining R_{ct} and C_{int} from Figs. 8b and 9a, respectively. The corresponding charge transfer relaxation times for Li transport were also calculated for a cathode of all-micrometric AR–LMO by using EIS data collected in an electrolyte of the same composition. These results for the AR sample (shaded bars) are plotted with those for the BM sample (open bars) in Fig. 11a. The general voltage-dependent trends for the two sets of these data are mutually comparable, but the overall values of τ_{ct} for the BM–LMO sample are noticeably smaller than those of the AR–LMO sample. This is a result of the large specific area and the dense packing of LMO nanoparticles that are responsible for the facile kinetic of reaction (1) in the BM cathode.

To obtain τ_d for the BM–LMO cathode (open bars in Fig. 11b), σ from Fig. 7b and C_{int} from Fig. 9a were combined in Eq. 7. The values of σ and C_{int} for the AR–LMO have been measured previously [2] and were used here in Eq. 7 to obtain τ_d for the all-micrometric LMO sample. The considerably larger values of τ_d found in the latter case are indicated by the shaded bars in Fig. 11b. A comparison of Fig. 11a, b indicates how the diffusion step of Li intercalation/de-intercalation is rate determining for reaction (1). The diffusion impedance, as measured in terms of σ in Fig. 7b, decreases in the intercalation voltage region [37], and thus, the voltage-dependent inclination of τ_d is almost opposite that of τ_{ct}.

As indicated in Eq. 5, full extraction of the energy stored in the Li|LMO half cell remains incomplete if T_{exp} drops below a threshold value, defined as τ_d. According to Fig. 11b, this latter time for the AR–LMO cathode is about 17 min through most of the intercalation region. The Ragone plot (a) in Fig. 5 also starts to rapidly drop along the specific energy axis, as the discharge duration of the cathode becomes smaller than this value (located between the diagonal lines for 5 and 30 min discharge steps). Similarly, the τ_d of ~30 s (open bars corresponding to 3.8, 4.1, and 4.2 V) for the BM–LMO corresponds well with the critical discharge time observed in Fig. 5 (between the 1 min and 10 s marking lines), where ε_s begins to decrease with increasing power densities on Ragone plot (b). These observed correlations between the galvanostatic Ragone plots and the EIS-measured diffusion times illustrate further how the considerations of material utilization, as noted in Eq. 5, govern the power delivery characteristics of the LMO cathodes.

Conclusions

Mechano-chemical modification by ball-milling is a convenient and relatively simple method of converting micrometric materials for Li ion battery electrodes to controlled mixtures of micro- and nanoparticles. The synergistic actions of this mixture can enhance both the rate capability and the cyclability of the processed material. The present study explores the electrochemical considerations of material utilization for supporting fast charge/discharge of LMO cathodes prepared in this approach. To do this, a phenomenological framework, adapted from earlier treatments of the problem [19, 24], is extended here to combine the results of EIS and galvanostatic measurements. The relative timescales for diffusion and charge transfer by Li⁺ in the LMO lattice are determined, and the effects of mechanical milling on these time parameters are examined. The results demonstrate how the nanoparticles in the BM material play a critical role in supporting fast charge/discharge.

References

1. Malik R, Burch D, Bazant M, Ceder G (2010) Nano Lett 10:4123–4127
2. Goonetilleke PC, Zheng JP, Roy D (2009) J Electrochem Soc 156:A709–A719
3. Lu C-H, Lin S-W (2001) J Power Sources 97–98:458–460
4. Ning L, Wu Y, Fang S, Rahm E, Holze R (2004) J Power Sources 133:229–242
5. Im D, Manthiram A (2003) Solid State Ionics 159:249–255
6. Morcrette M, Gillot F, Monconduit L, Tarascon J-M (2003) Electrochem Solid-State Lett 6:A59–A62
7. Thackeray MM, Johnson CS, Vaughey JT, Li N, Hackney SA (2005) J Mater Chem 15:2257–2267
8. Cabana J, Valdés-Solís T, Palacín MR, Oró-Solé J, Fuertes A, Marbán G, Fuertes AB (2007) J Power Sources 166:492–498
9. Sun X, Yang XQ, Balasubramanian M, McBreen J, Xia Y, Sakai T (2002) J Electrochem Soc 149:A842–A848
10. Zheng JP, Crain DJ, Roy D (2011) Solid State Ionics 196:48–58
11. Kang S-H, Goodenough JB, Rabenberg LK (2001) Chem Mater 13:1758–1764
12. Soiron S, Rougier A, Aymard L, Tarascon J-M (2001) J Power Sources 97–98:402–405

13. Kang SH, Goodenough JB, Rabenberg LK (2001) Electrochem Solid-State Lett 4:A49–A51
14. Jang DH, Oh SM (1997) J Electrochem Soc 144:3342–3348
15. Zheng JP (2009) Clarkson University, PhD Thesis
16. Van der Ven A, Marianetti C, Morgan D, Ceder G (2000) Solid State Ionics 135:21–32
17. Liu W, Kowal K, Farrington GC (1998) J Electrochem Soc 145:459–465
18. Verbrugge MW, Koch BJ (1999) J Electrochem Soc 146:833–839
19. Rougier A, Striebel KA, Wen SJ, Cairns EJ (1998) J Electrochem Soc 145:2975–2980
20. Zhang D, Popov BN, White RE (2000) J Electrochem Soc 147:831–840
21. Zhang SS, Xu K, Jow TR (2002) Electrochem Solid State Lett 5:A92–A94
22. Guyomard G, Tarascon JM (1993) J Electrochem Soc 140:3071–3081
23. Edström K, Gustafsson T, Thomas JO (2004) Electrochim Acta 50:397–403
24. Doyle M, Fuller TF, Newman J (1993) J Electrochem Soc 140:1526–1533
25. Huang H, Vincent CA, Bruce PG (1999) J Electrochem Soc 146:3649–3654
26. Bazito FFC, Torresi RM (2006) J Braz Chem Soc 17(2006):627
27. Srinivasan V, Newman J (2004) J Electrochem Soc 151:A1530–A1538
28. Bao SJ, Liang YY, Li HL (2005) Electrochim Acta 59:3761–3765
29. Sheng Shui Z (2007) J Power Sources 163:713–718
30. Hjelm A (2002) Electrochim Acta 47:1747–1759
31. Pyun SI, Choi YM, Jeng ID (1997) J Power Sources 68:593–599
32. Rho Y, Dokko K, Kanamura K (2006) J Power Sources 157:471–476
33. Lu D, Li W, Zuo X, Yuan Z, Huang Q (2007) J Phys Chem C 111:12067–12074
34. Arora P, Popov BN, White RE (1998) J Electrochem Soc 145:807–815
35. Zheng JP, Moganty SS, Goonetilleke PC, Baltus RE, Roy D (2011) J Phys Chem C 115:7527–7537
36. Sluyters-Rebach M, Sluyters JH (1970) Sine wave methods in the study of electrode processes. In: Bard AJ (ed) Electroanalytical chemistry, vol 4. Dekker, New York, pp 3–128
37. Aurbach D, Levi MD, Levi E, Teller H, Markovsky B, Salitra G, Heider U, Heider L (1998) J Electrochem Soc 145:3024–3034